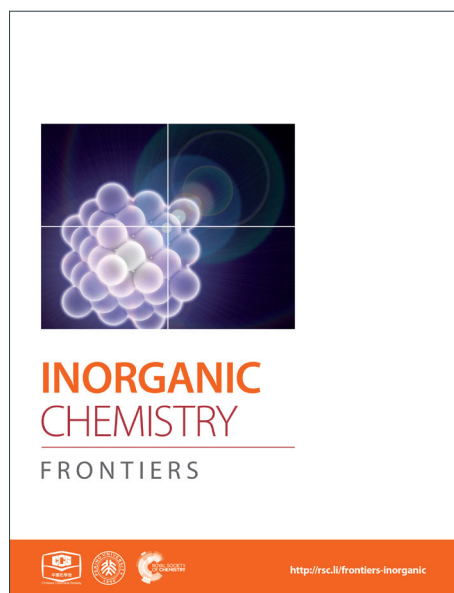
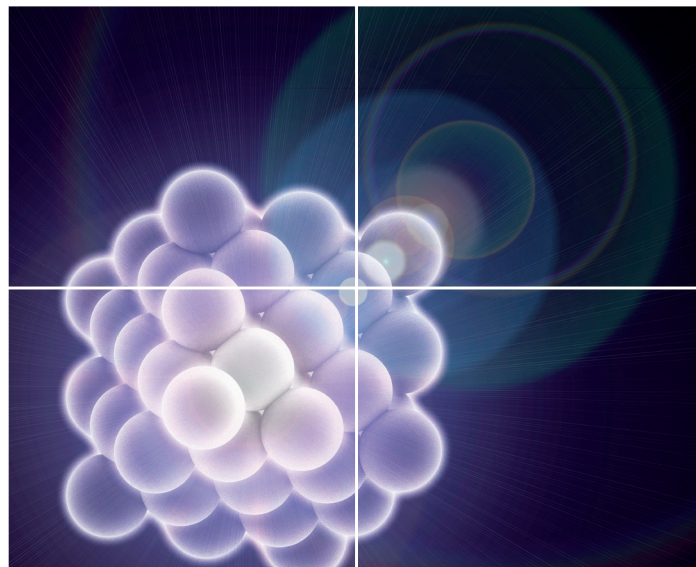


INORGANIC CHEMISTRY

FRONTIERS

Accepted Manuscript



This is an *Accepted Manuscript*, which has been through the Royal Society of Chemistry peer review process and has been accepted for publication.

Accepted Manuscripts are published online shortly after acceptance, before technical editing, formatting and proof reading. Using this free service, authors can make their results available to the community, in citable form, before we publish the edited article. We will replace this *Accepted Manuscript* with the edited and formatted *Advance Article* as soon as it is available.

You can find more information about *Accepted Manuscripts* in the [Information for Authors](#).

Please note that technical editing may introduce minor changes to the text and/or graphics, which may alter content. The journal's standard [Terms & Conditions](#) and the [Ethical guidelines](#) still apply. In no event shall the Royal Society of Chemistry be held responsible for any errors or omissions in this *Accepted Manuscript* or any consequences arising from the use of any information it contains.

Designing Syntheses and Photophysical Simulations of Noncentrosymmetric Compounds

Wen-Dan Cheng,* Chen-Sheng Lin, Zhong-Zhen Luo, Hao Zhang

*State Key Laboratory of Structural Chemistry, Fujian Institute of Research on the Structure of Matter, Chinese Academy of Sciences, Fuzhou, Fujian, 350002, PRC.
Fax:(+86)591-83714946,Tel:(+86)591-83713068. E-Mail: cwd@fjirsm.ac.cn*

Abstract

In this paper, we describe the preparations of inorganic noncentrosymmetry (NCS) chalcogenides and their infrared nonlinear optical properties. We present a reasonable synthesis of inorganic NCS compounds by thinking of genetic development processes of a living organism. The basic unit having NCS structure is selected as a chromophore of NCS materials. The NCS compounds will be obtained from NCS chromophore development of normal growth. The chromophore development will be an alienation process of growth if the NCS compound is not formed by NCS chromophore. The normal developments of the NCS chromophores (SnS_4) and (Sn_2S_3) obtain the NCS crystal of $\text{Ba}_7\text{Sn}_5\text{S}_{15}$; and the normal developments of the NCS chromophores of (BiS_5) and (InS_4) obtain a compound of $\text{Ba}_2\text{BiInS}_5$ keeping in NCS structure. Both of them, the Ba^{2+} ions are a charge-compensating agent. The NCS crystals SnGa_4Q_7 ($\text{Q} = \text{S}, \text{Se}$) were obtained by NCS chromophores of (GaQ_4) and (SnQ_4). However, the centrosymmetry (CS) compound of $\text{Ba}_6\text{Sn}_7\text{S}_{20}$ was obtained because the developments of NCS chromophores of the (SnS_4) and (SnS_5) alienate from the normal process of growth. We give more examples of NCS chromophore developments of normal and alienable processes in this paper. For NCS compounds, we have searched their nonlinear optical (NLO) properties of micro-crystals (powders) and electronic origin of NLO response. The intensity of second harmonic generation (SHG), laser-induced damage threshold (LIDT), and infrared transparency were measured, and the conversion efficiency, figure of merit (FOM), and energy band structure were calculated for these NCS compound materials. It is found that the NCS materials of SnGa_4Q_7 ($\text{Q} = \text{S}, \text{Se}$) appear with large conversion efficiencies, high damage threshold and wide transparencies in the mid-infrared region. And, the study of micro-mechanism elucidate that the stereochemically active lone-pair electrons of Sn^{2+} can significantly improve the polarity of the [SnQ_4] chromophore. Large NLO responses of them originate from the covalent interactions of Sn-Q and the cooperative effects of polarities between the chromophore [SnQ_4] and [GaQ_4]. It is also found that the $\text{Ba}_7\text{Sn}_5\text{S}_{15}$ material is type-I phase-matchability, and that the SHG conversion efficiency and FOM is about twice of that of AgGaS_2 at the saturated particle size (particle size of 150–212 μm). The $\text{Ba}_8\text{Sn}_4\text{S}_{15}$ is not phase-matching material. The SHG intensity and conversion efficient of $\text{Ba}_8\text{Sn}_4\text{S}_{15}$ are separately about 250 times than those of $\alpha\text{-SiO}_2$, and the SHG intensity and conversion efficient

are separately about 10 times than those of AgGaS₂ at the particle size of 25–45 μm.

Introduction

The noncentrosymmetric (NCS) compounds and their crystals can exhibit a variety of technologically important physical properties, and the NCS crystals may become the materials of piezoelectricity, pyroelectricity, ferroelectricity, and second-order nonlinear optical (NLO) response¹. The structural symmetry of material affects its property. There are the crystallographic interrelationships between the NCS crystal classes^{2,3} and physical properties, and among 32 crystal point groups⁴, 20 NCS groups (21 NCS crystal classes excluding point group 432 (O group)) can exhibit the piezoelectric or NLO effect. It is noted that all pyroelectric materials have NLO behavior but the converse is not true. The NLO material can be made into optical frequency conversion device, and it can broaden the wavelength coverage ranges of laser spectrum. As well known, one can distinguish between two classes of laser sources⁵. One class includes sources which generate tunable laser radiation directly from gain in gas discharge, solid-state bulk materials or optical fibers, i.e. direct laser radiation sources. The longest wavelength coverage of direct solid state laser source is only limited under 3.5 microns. The other class of laser sources is based on frequency conversion of basic laser sources by using NLO crystal. It is for this purpose that many NLO crystals have been developed to broaden the wavelength coverage of laser spectrum. Scientists and engineers constantly explore new NLO material to solve the development of optical technology demand and twenty-first century scientific and technologic challenges. The main progress took place in the last two decades following the advancement in near-infrared solid state laser technology and NLO crystals. The second harmonic generation (SHG), parametric down-conversion and up-conversion processes in NLO crystals as well as combinations of them have been widely used to fill in gaps in the laser spectrum, in which the direct laser radiations do not exist or certain operational regimes are impossible from the vacuum ultraviolet (~150 nm) to the deep mid-IR (middle infrared)⁶⁻⁹. The coherent mid-IR sources have important applications in sciences and technology, including the detection and quantification of molecular trace gases¹⁰, medical diagnostics and military systems¹¹⁻¹², free space optical communication and deep space exploration, etc^{5,13-14}.

At present, nonlinear frequency down-conversion is still a powerful method to transform the wavelength of near-IR laser sources to the mid-IR spectral range and generate coherent radiation in all time zones from 3 μm up to 20 μm and above. Non-oxide NLO crystals play key role, in particular above 5 μm, such as unary, binary, ternary and quaternary arsenides, phosphides, sulfides, selenides or tellurides, and they have been used in such down-conversion devices. During the past ten years, many compounds with large NLO coefficients and wide transparencies in IR regions have been prepared, and they are K₂P₂Se₆¹⁵, Na₂Ge₂Se₅¹⁶, K₄GeP₄Se₁₂¹⁷, Na_{0.5}Pb_{1.75}GeS₄¹⁸, LiGaGe₂Se₆¹⁹, α- and β-A₂Hg₃M₂S₈ (A = K, Rb; M = Ge, Sn)²⁰, Li₂In₂GeSe₆²¹, Li₂CdMS₄ (M = Ge, Sn)²², Ba₆Sn₆Se₁₃²³, [Zn(H₂O)₄][Zn₂Sn₃Se₉(MeNH₂)]²⁴, K₆Cd₄Sn₃Se₁₃²⁵, K₁₄Cd₁₅Sn₁₂Se₄₆

²⁶, $A_6Sn[Zn_4Sn_4S_{17}]$ ($A = K, Rb, Cs$)²⁷, $BaGa_2GeQ_6$ ($Q = S, Se$)²⁸, $Pb_4Ga_4GeQ_{12}$ ($Q = S, Se$)²⁹, $Ba_4CuGa_5Q_{12}$ ($Q = S, Se$)³⁰, $Ag_2In_2Si(Ge)S_6$ ³¹, $Ag_{0.5}Pb_{1.75}Ge(S_{1-x}Se_x)_4$ ³², $Zn_xBa_2B_2S_{5+x}$ ($x \approx 0.2$)³³, $CsCd_4X^{III}_5Q_{12}$ ($X^{III} = Ga, In; Q = S, Se$)³⁴, and $Rb_2CdBr_2I_2$ ³⁵. All of them have their specific advantages but also some drawbacks. The crystals of $AgGaS_2$, $AgGaSe_2$, $ZnGaP_2$, $GaSe$ and $CdSe$ also have some drawbacks although they can be obtained from the commercial market³⁶. The crystals of $AgGaS_2$ and $AgGaSe_2$ have residual absorption, poor thermal conductivity and anisotropic thermal expansion. The crystal of $ZnGaP_2$ has a limited transparency due to multi-photon and residual absorption. $GaSe$ crystal is very low damage threshold, and $CdSe$ has quite modest birefringence and nonlinearity. Accordingly, the development of new and improvement of existing nonlinear crystals are critical for advancing mid-IR coherent source, at particular, with increasing conversion efficiency and the output power.

Drs. I. Chung and M. G. Kanatzidis considered that the metal chalcogenides are the most promising source of potential NLO materials with desirable properties, particularly in the IR region³⁷. A general strategy is suggested to employ NCS chromophore as building units in the design syntheses of NLO crystals³⁸⁻⁴⁰. The NCS chromophore include the distorted polyhedron with a d^0 cation center resulting from a second-order Jahn-Teller (SOJT) effect⁴¹⁻⁴⁴, polar displacement of a d^{10} cation center⁴⁵, and stereochemically active lone pair (SCALP) effect of cation⁴⁶⁻⁴⁸, and the distorted triangle and tetrahedron^{49-52a}. The NLO crystal materials can be also constructed by the multifold NCS chromophore with different coordinate environments^{52b,53}. In this paper, we present the reasonable designs of mid-IR NCS crystals by thinking of gene development process.

Designs and Syntheses of Noncentrosymmetric Compounds

Optimization of material chromophore

NCS chromophore is a fundamental building block (FBB) toward a NCS material. The development of NCS chromophore will produce an instrument device, which is along the processes: chromophore \rightarrow cluster \rightarrow ... \rightarrow unit cell \rightarrow single crystal \rightarrow device. In bio-system, genetic development is along the processes: gene \rightarrow genome \rightarrow ... \rightarrow cell \rightarrow tissue \rightarrow organ. There are some common factors between a gene and NCS chromophore; both are the developments from a basic unit toward a larger purpose of dimension and function. However, their natures are different. A gene is the molecular unit of heredity of a living organism, and it holds the information to build and maintain an organism's cell and pass genetic traits to offspring. The word gene, when applied in non-biological contexts, connotes a FBB toward a larger purpose⁵⁴. Here, we must have a clear understanding that the material chromophore is not life activity and the gene in bio-system is consisted in vital organ. By thinking of gene development in biosystem, we present the reasonable designs of NCS inorganic materials originating from NCS chromophores. A NCS chromophore of material has different coordinate structures, and they are the distorted triangle, pentagon, n-polygon (n is odd number with $\neq 1$), tetrahedron, octahedron, square pyramid, pentagonal pyramid, triangular bipyramid, pentagonal bipyramid, and other NCS structure geometry, as shown in Figure 1.1.

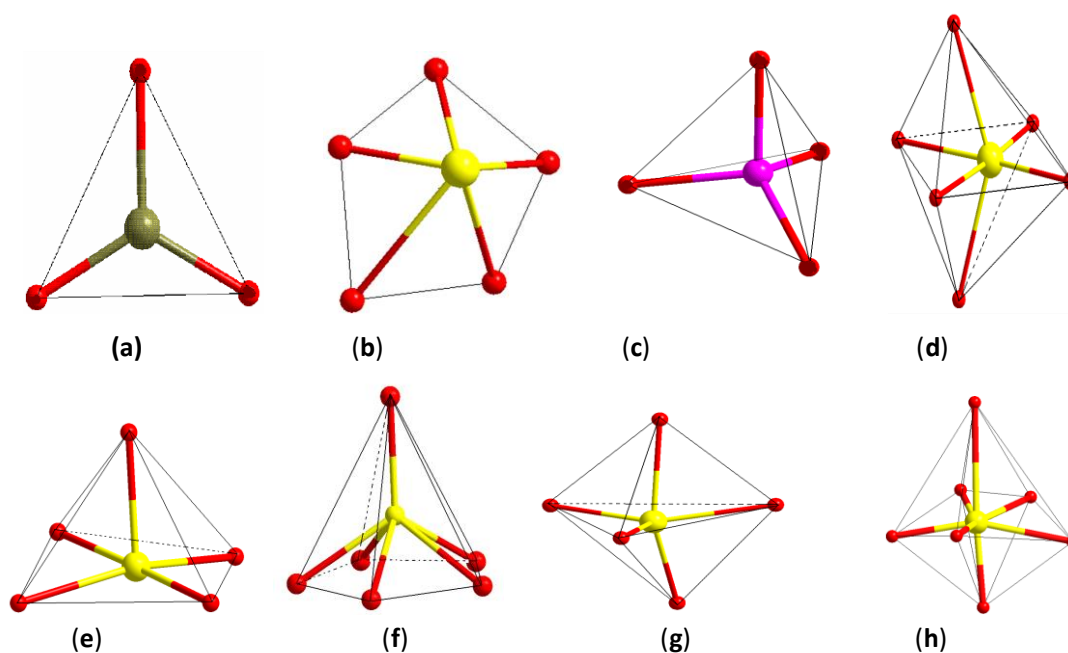


Figure 1.1 Noncentrosymmetric chromophore structures. (a) non-equilateral triangle (or triangular pyramid), (b) non-equilateral pentagon, (c) tetrahedron, (d) distortion octahedral, (e) square pyramid, (f) pentagonal pyramid, (g) triangular bipyramid, (h) pentagon bipyramid.

It is no guarantee to predict a macroscopically NCS material which is the development from NCS chromophore. A NCS chromophore will develop gradually with a normal process of growth if the NCS crystal is constructed by using NCS chromophore. The chromophore development will be an alienation process of growth if the NCS structural crystal is not formed by NCS chromophore. Such cases have been carefully studied by several groups. Dr. Poepelmeier *et al.*⁵⁵⁻⁵⁹ synthesized and examined the crystallographically ordered transition-metal oxyfluorides $[\text{MO}_x\text{F}_{6-x}]^{n-}$ ($M=d^0$ transition metal, $x = 1-3$, and $n = 2, 3$) and determined that the polar or no polar symmetry originates from the changes in the bond network. Dr. Halasyamani *et al.* studied another series of analogues $\text{A}_2\text{Ti}(\text{IO}_3)_6$ ($\text{A}=\text{Li, Na, K, Rb, Cs, Tl}$) and considered that the polarity results only from the Li and Na phases of cation-size, coordination requirements, and bond valence concept arguments⁶⁰. Our group synthesized CS crystal of $\text{Ba}_2\text{BiGaS}_5$ and NCS crystal of $\text{Ba}_2\text{BiInS}_5$ and they are constructed by tetrahedron (Ga/InS_4) chromophore and square-pyramidal (BiS_5) chromophore⁶¹, and we consider that the different crystal symmetries result from the distorted tetrahedron or cation size effect in these two compounds.

CS materials of $\text{Ba}_6\text{Sn}_7\text{S}_{20}$, $\text{Ba}_2\text{BiGaS}_5$ and NCS materials of $\text{Ba}_7\text{Sn}_5\text{S}_{15}$, $\text{Ba}_2\text{BiInS}_5$

Compound $\text{Ba}_7\text{Sn}_5\text{S}_{15}$ was prepared by a solid-state reaction method from stoichiometric amounts of BaS, Sn, and S. It crystallizes in NCS space group $P6_3\text{cm}$ of the hexagonal system, and is constructed by the material chromophores of tetrahedron (SnS_4) and triangular pyramid (SnS_3)⁶². The Sn-S distances vary from 2.361 to 2.407 Å in the SnS_4 tetrahedron, and the calculated bond valence sums (BVS) of the Sn is 4.27 or 4.14, which is close to the oxidation state +4 of Sn. In the triangular pyramidal (SnS_3), the Sn is a threefold coordination with Sn-S distances

ranging from 2.583 to 2.687 Å, and the calculated BVS is 2.30 or 2.25 which is close to oxidation state of +2. The two triangular pyramids (2SnS_3) are the arrangements against each other. They are share with a basal plane and form a triangular bipyramid (Sn_2S_3). The isolated $[\text{SnS}_4]^{4-}$ tetrahedra and $[\text{Sn}_2\text{S}_3]^{2-}$ triangular bipyramids held together by the Ba^{2+} cations⁶². The NCS chromophores of (SnS_4) and (Sn_2S_3) develop normally into NCS crystal, the skeleton frame is plotted in Figure 1.2a. Compound $\text{Ba}_6\text{Sn}_7\text{S}_{20}$ was prepared with the molar ratio of stoichiometric amounts from Ba, Sn, and S. It crystallizes in CS space group $C2/c$ of the monoclinic system, and is constructed by the material chromophores of tetrahedron (SnS_4) and triangular bipyramid (SnS_5)⁶². In the triangular bipyramid, the Sn atom is coordinated by five S atoms with Sn-S distances ranging from 3.339 to 3.812 Å, and the calculated BVS of Sn is 4.09 or 3.96 which is close to oxidation state +4 of Sn. In the SnS_4 tetrahedron, the Sn-S distances vary from 2.327 to 2.481 Å and the calculated BVS of Sn is 3.99 or 4.04, which is also close to the oxidation state +4 of Sn. Three (SnS_4) tetrahedrons are connected to each other by corner sharing to form a kind of basic structural unit $[\text{Sn}_3\text{S}_8]^{4-}$, and four (SnS_5) triangular bipyramids are connected to each other by edge sharing to form another basic structural unit $[\text{Sn}_4\text{S}_{14}]^{12-}$. Both of the structural units $[\text{Sn}_3\text{S}_8]^{4-}$ and $[\text{Sn}_4\text{S}_{14}]^{12-}$ are connected to each other by corner sharing to form a three-dimensional framework with the Ba cations in the cavities in the configuration of the $\text{Ba}_6\text{Sn}_7\text{S}_{20}$ ⁶². The developments of NCS chromophores of the (SnS_4) and (SnS_5) alienate from the normal process of growth, and the CS crystal is obtained as shown in Figure 1.2b. By the comparisons between these two processes, we consider that the different crystal symmetries between the $\text{Ba}_6\text{Sn}_7\text{S}_{20}$ and $\text{Ba}_7\text{Sn}_5\text{S}_{15}$ result from the different oxidation states of Sn ion. We believe that the low oxidation state of Sn ions in the material chromophore (Sn_2S_3) will be favorable for growing NCS crystal.

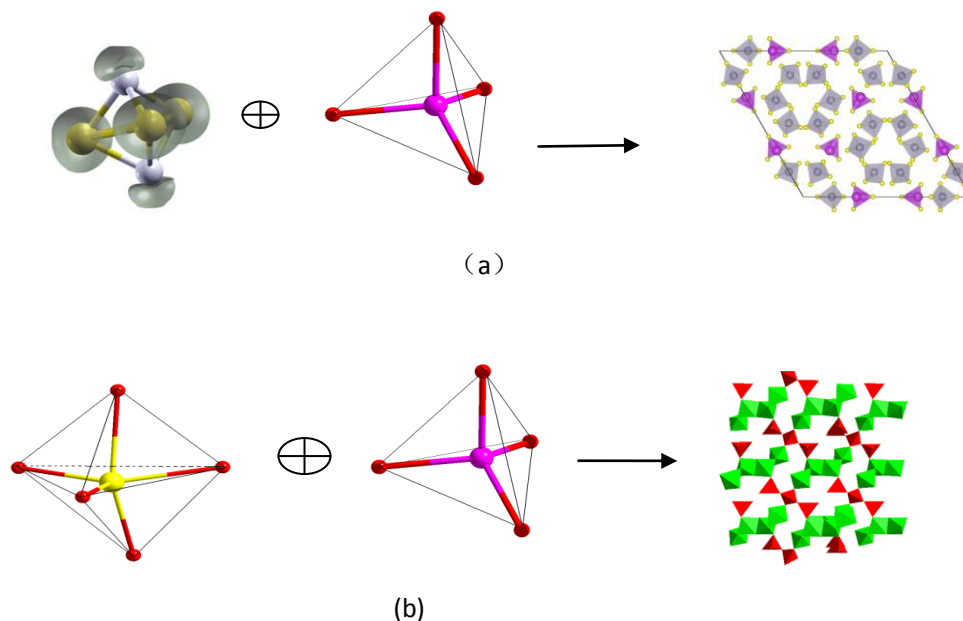
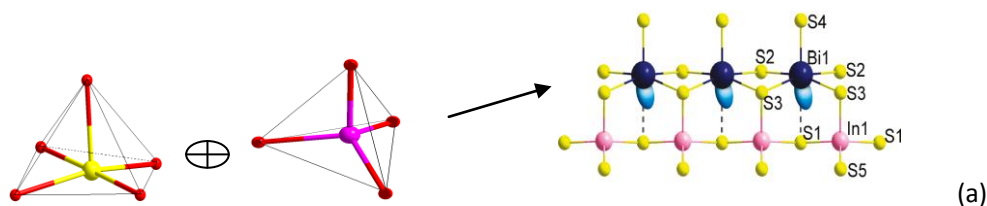


Figure 1.2. The skeleton frame of NCS chromophore developments (no shown Ba^{2+} ions), (a) normal process of chromophores (SnS_5) and (SnS_4) into $\text{Ba}_7\text{Sn}_5\text{S}_{20}$; (b) alienated process of growth into material $\text{Ba}_6\text{Sn}_7\text{S}_{20}$ from chromophores (SnS_5) and (SnS_4).

Compound $\text{Ba}_2\text{BiInS}_5$ was prepared by a solid-state reaction method from stoichiometric amounts of BaS, Bi, In, and S. It crystallizes in NCS space group $Cmc2$ of the orthorhombic system, and is constructed by the NCS chromophores of the tetragonal pyramid (BiS_5) and tetrahedron (InS_4), and charge-compensating Ba^{2+} ion⁶¹. The Bi^{3+} ion is coordinated by five S^{2-} ions, and the bond lengths of Bi--S vary from 2.582(5) to 2.959(4) Å, featuring the irregular tetragonal pyramid (BiS_5). In the tetrahedron (InS_4), the In^{3+} ion is coordinated by four S atoms in the tetrahedral arrangement with bond lengths ranging from 2.447(6) to 2.578(6) Å. The edge-shared BiS_5 tetragonal pyramids with parallel arrangements are formed into a chain, and the corner-shared InS_4 tetrahedrons are also formed into a chain. These two chains are further interconnected with each other through sharing corner to form the whole $1^\infty[\text{BiInS}_5]^{4-}$ anionic chain. The NCS chromophores of (BiS_5) and (InS_4) develop into a compound keeping in NCS structure, as shown in Figure 1.3a. Compound $\text{Ba}_2\text{BiGaS}_5$ was prepared by a solid-state reaction method from stoichiometric amounts of BaS, Bi, Ga, and S. It crystallizes in CS space group $Pnma$ of the orthorhombic system, and is constructed by the NCS chromophores of the tetragonal pyramid (BiS_5) and tetrahedron (GaS_4), and charge-compensating Ba^{2+} ion⁶¹. The coordinate environments of chromophores (BiS_5) and (GaS_4) in the CS crystal $\text{Ba}_2\text{BiGaS}_5$ are the same as those in the NCS crystal $\text{Ba}_2\text{BiInS}_5$. In the CS crystal $\text{Ba}_2\text{BiGaS}_5$, however, the edge-shared BiS_5 tetragonal pyramids with anti-parallel arrangements are formed into a chain, and the tetrahedron GaS_4 is connected with the tetragonal pyramid BiS_5 by the sharing corner and the tetrahedrons are the alternate arrangements along the chain constructing by the BiS_5 . Furthermore, they form an infinite one-dimensional (1D) $1^\infty[\text{BiGaS}_5]^{4-}$ anionic chain. The developments of the NCS chromophores appear in the alienated process and obtain the CS crystal $\text{Ba}_2\text{BiGaS}_5$, as shown in Figure 1.3b. It is a very interesting that the different crystal symmetries between the CS $\text{Ba}_2\text{BiGaS}_5$ and NCS $\text{Ba}_2\text{BiInS}_5$ are obtained from the same coordinate structure of NCS chromophores of tetrahedron ($\text{GaS}_4/\text{InS}_4$) and tetragonal pyramid (BiS_5). We check the configurations of these two crystals in details. A small size GaS_4 is connected with the neighboring BiS_5 through edge-sharing. This situation leads to a *trans* arrangement along the $1^\infty[\text{BiGaS}_5]^{4-}$ chain with the apexes of BiS_5 pyramids reversed up and down alternately, and results in the CS nonpolar structure of compound $\text{Ba}_2\text{BiGaS}_5$. A large size InS_4 is connected with the neighboring BiS_5 through corner-sharing and it results in *cis* arrangement along the $1^\infty[\text{BiInS}_5]^{4-}$ anionic chain with the parallel apexes of BiS_5 pyramids, and obtains the NCS polar structure of $\text{Ba}_2\text{BiInS}_5$.



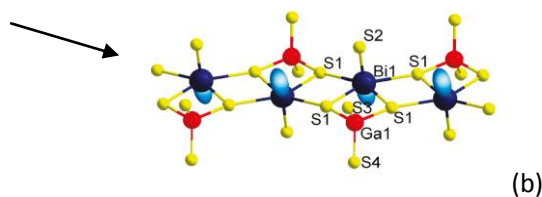


Figure 1.3. The skeleton frame of NCS chromophore developments (no shown Ba^{2+} ions), (a) normal process of growth from chromophores (BiS_5) and (InS_4) into material $\text{Ba}_2\text{BiInS}_5$; (b) alienated process of growth from chromophores (BiS_5) and (GaS_4) into material $\text{Ba}_2\text{BiGaS}_5$.

NCS materials of SnGa_4Q_7 ($\text{Q} = \text{S}, \text{Se}$) and $\text{Ba}_8\text{Sn}_4\text{S}_{15}$ with Sn-Q covalent interactions

Compounds SnGa_4S_7 and SnGa_4Se_7 were prepared from reactants of Sn, Ga, and S/Se by a solid-state reaction method at high temperature, respectively. Both compounds are crystallize in NCS space group Pc of the monoclinic system, the remarkable configurations of three dimension frameworks are formed by the tetranuclear secondary basic structure unit Ga_4Q_{11} which is constructed by four GaQ_4 tetrahedrons, and the SnQ_4 tetragonal pyramid locating in the cavities⁶³. In other words, the NCS crystals SnGa_4Q_7 ($\text{Q} = \text{S}, \text{Se}$) are constructed by NCS chromophores of tetrahedron (GaQ_4) and tetragonal pyramid (SnQ_4), as plotted in Figure 1.4. The Sn atom is bonded to four Q atoms at two short and two long distances, forming the SnQ_4 tetragonal pyramid, and the Sn-S bond distances range from 2.654 to 2.992 Å in the SnGa_4S_7 and the Sn-Se bonds vary from 2.773 to 3.111 Å in the SnGa_4Se_7 . All Ga sites are coordinated by four Q atoms to form the tetrahedrons GaQ_4 . The Ga-S bond lengths range from 2.214 to 2.337 Å in the SnGa_4S_7 and the Ga-Se bonds vary from 2.346 to 2.463 Å in the SnGa_4Se_7 . The atomic covalent radius of S, Se, and Sn are individually 1.05(3), 1.20(4), and 1.39 (4) Å⁶⁴, and here, the bond lengths of Sn-S and Sn-Se are little larger than the sum of covalent radius due to the crowd coordination environments of SnG_4 ($\text{G} = \text{S}, \text{Se}$). The calculated ELF (electron localization function) plot shows that there is a charge distribution along the bond axis of Sn-Se (Figure 1.5a). This finding indicates the Sn-Se covalence interactions.

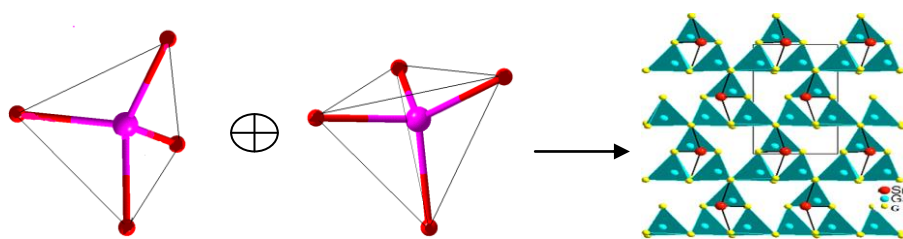


Figure 1.4. The skeleton frame of NCS chromophore developments of normal process from (SnS_4/Se_4) and (GaS_4/Se_4) into NCS materials of SnGa_4Q_7 ($\text{Q} = \text{S}, \text{Se}$).

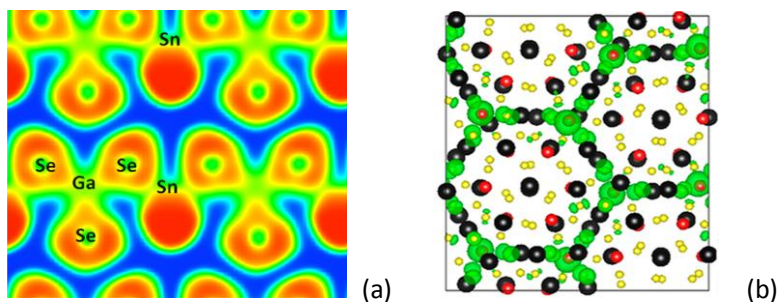


Figure 1.5. (a) The electron localization function map of SnGa_4Se_7 at (001) plane cutting through the Sn and Ga atoms and the electron localization function value ranging from 0 (blue) to 1 (red); (b) the charge distributions of the occupied bands nearby the Fermi level for $\text{Ba}_8\text{Sn}_4\text{S}_{15}$ (black, Ba; red, Sn; yellow, S).

Compound $\text{Ba}_8\text{Sn}_4\text{S}_{15}$ was prepared from a stoichiometric mixture of the $\text{BaS}/\text{SnS}/\text{SnS}_2$ by a solid-state reaction method at high temperature, and it crystallizes in the NCS space group $Pca2_1$ of orthorhombic system⁶⁵. The $\text{Ba}_8\text{Sn}_4\text{S}_{15}$ crystal is constructed by the NCS chromophores of tetrahedrons (SnS_4) and pyramids (SnS_3) with Ba^{2+} cations inserting between them for charge balance. Figure 1.6 gives the skeleton frame of chromophore developments of normal process from NCS chromophores (SnS_3) and (SnS_4). In the tetrahedrons SnS_4 , the Sn-S distances range from 2.3373 to 2.4124 Å, and the calculated BVS of Sn is 4.20 or 4.09 which is close to oxidation state +4; in the SnS_3 pyramids, the Sn-S bond lengths range from 2.5336 to 2.6817 Å, and the calculated BVS of Sn is 1.93 which is close to oxidation state +2⁶⁵. At the right of figure 1.6, the secondary basic structure unit of $\text{Ba}_8\text{Sn}_4\text{S}_{15}$ is regarded as a coin-like structure, which forms the two-dimensional (2D) honeycomb structure by alternate arrangement in parallel. The skeleton of the honeycomb (coin-like configuration) is formed by 6 SnS_3 pyramidal units and 18 Ba atoms in the ordered arrangement on the edge and isolated nine SnS_4 tetrahedral units and eight Ba atoms fill in the cells of the honeycomb. The charge distributions near the Fermi level are main contributions from SnS_3 pyramidal units, shown in figure 1.5b. This finding also indicates the Sn-S covalent interaction in SnS_3 .

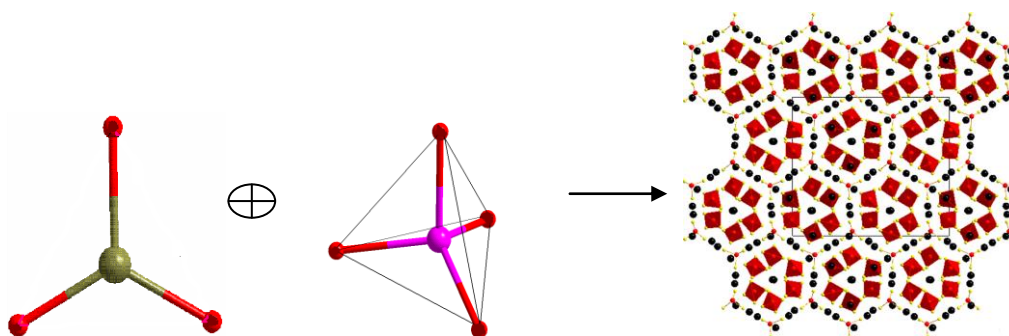


Figure 1.6. The skeleton frame of NCS chromophore developments of normal process from chromophores (SnS_3) and (SnS_4) into NCS material of $\text{Ba}_8\text{Sn}_4\text{S}_{15}$

Photophysics Simulations and Micro-Mechanisms of Infrared NLO Materials

Physical properties

The optical conversion efficiency is the most important standard to evaluate optical property of NLO materials. While we select a NLO crystal as frequency conversion devices with a certain laser wavelength, the first option is to require high conversion efficiency. For simplicity of representation, we only consider the SHG process of NLO response. The SHG conversion efficiency is defined as $\eta = I_{2\omega}/I_{\omega}$, which is a rate of SHG and incident light intensities. The SHG intensity $I_{2\omega}$ can be written in terms of the intensity of the incident field according to the couple wave theory, and the expression is written as following^{66a}:

$$I_{2\omega} = \frac{32d_{\text{eff}}^2 \omega^2 I_{\omega}^2}{n_{\omega}^2 n_{2\omega} \epsilon_0 c^2} L^2 \frac{\sin^2(\Delta k L / 2)}{(\Delta k L / 2)^2} \quad (1).$$

In the MKS system, we can write the conversion efficiency as

$$\eta = C \cdot FOM \cdot I_{\omega} L^2 \lambda_{\omega}^{-2} \cdot PMF, \quad (2);$$

in which the *PMF* is phase mismatch factor, which includes entirely the effect of wave vector, the constant $C = 128\pi^2 \epsilon_0^{-1}$, the $FOM = d_{\text{eff}}^2 (n_{\omega}^{-2} n_{2\omega}^{-1})$ is defined as a figure of merit. Here, the relative of $\omega = 2\pi c/\lambda$ is employed from formula (1) to (2). In accordance with formula (2), to maximize the SHG efficiency it is essential that the condition of perfect phase matching is satisfied, i.e. $\Delta k \rightarrow 0$ and $PMF = 1$, otherwise, it is a dramatic decrease in the SHG efficiency. Under the condition of $PMF = \sin^2(\Delta k L / 2) \cdot (\Delta k L / 2)^{-2}$ perfect phase matching, the SHG efficiency can be improved by using higher radiation intensity I_{ω} and shorter radiation wavelength λ_{ω} , longer interaction length L , and greater figure of merit FOM . The powder SHG conversion efficient of a new material can be determined by comparisons with standard material in terms of the measurements of SHG intensity vs particle size^{63,68}.

FOM is determined by the SHG coefficient d and refractive index n of material, and they can be simulated or calculated by the energy band theory combining with sum-over-states method⁶⁷ or classical anharmonic oscillator model^{66b}. The bulk SHG coefficient, d_{eff} , can be estimated by the comparisons between the incident optical intensities of the sample and known material⁶⁸. The optical parameters d and n are related to the space structure, charge distribution and transition energy of crystal material. The FOM is a primary index for screening of different NLO materials.

Radiation intensity I_{ω} is dependence on the incident optical power P at the fundamental frequency and the cross-sectional area A , and it is in accordance with the relation of $I_{\omega} = P/A$. Accordingly, to obtain the strongest radiation intensity, there must have the largest possible power P and the smallest possible area A if the threshold of the NLO crystal is not a limiting factor. In fact, this situation is not possible, and the threshold is dependent on optical gap of material. The latter can be obtained by the calculation of band structures or the measurement of UV-vis diffuse

reflectance spectra⁶⁹.

Additionally, the SHG efficiency can be improved if there has a large ratio L/λ_ω . To obtain a large ratio L/λ_ω , it requires light pass the journey of crystal as long as possible or a large size of crystal and provide a shorter incident wavelength. For a thick crystal (a large L), the maximum ratio L/λ_ω for a given wavelength λ_ω is limited by thermal conductivity of material (low thermal conduction will lead to the heat accumulation and the crystal burst within a large size of crystal). For a thin crystal (very small L), to obtain a large ratio L/λ_ω requires radiation wavelength as short as possible. It is limiting by the given wavelength of radiation source and the anti-damage ability of material. Accordingly, we require a wide window of light transparence in NLO materials. This fact allows to have a wide coverage of the tunable incident wavelength.

The NLO crystal with high quality laser frequency conversion must meet the conditions of strong radiation intensity I_ω , short radiation wavelength λ_ω , long interaction length L , and great figure of merit FOM, which associates with high conversion efficient. Additionally, NLO crystals require: (1) the stability of physical and chemical properties, high hardness, anti-moisture; (2) a good optics uniformity of large size crystal; (3) easy processing and low price for crystal, etc. In fact, it is very few that the NLO crystal is in full compliance with the terms mentioned above. We only select the NLO crystal that meets the most basic conditions according to the application requirement. For example, we require a high conversion efficient, a large FOM , width infrared transparence including two windows of atmosphere (about 4 and 16 μm), and large threshold for infrared NLO crystals.

Phase matching requirement

Figure 2.1a shows a plot of the SHG intensity vs. particle size for SnGa_4G_7 powders ($G = \text{S}, \text{Se}$), and the AgGaS_2 powder was prepared with the same size ranges as the reference⁶³. The SHG intensities of these powders are essentially proportional to particle sizes, which indicate that they are the type-I phase-matching materials⁷⁰. The Type-I phase matching represents that the polarizations of both two input beams at ω frequencies are parallel to each other, and the polarization of output beam at 2ω is orthogonal to input beams. In accordance with formula (2), phase-matching requirement is essential to maximize the SHG efficiency. Furthermore, we can derive the relative SHG conversion efficiencies $\eta^S/\eta^R = (I_{2\omega}^S/I_\omega)/(I_{2\omega}^R/I_\omega)$ from the relative SHG intensities $I_{2\omega}^S/I_{2\omega}^R$ between sample and reference. From figure 2.1a, we can find that the SHG intensities of SnGa_4S_7 and SnGa_4Se_7 are about 1.3 and 3.8 times than that of the benchmark AgGaS_2 at the particle size of 150–210 μm , respectively. These findings indicate that the conversion efficiencies of SnGa_4G_7 ($G = \text{S}, \text{Se}$) are 1.3 and 3.8 times larger than that of those of AgGaS_2 , separately, under the same experimental conditions and devices. Figure 2.1b gives the plots of the SHG intensity of particle-size dependence for $\text{Ba}_8\text{Sn}_5\text{S}_{15}$ powders. It shows the important feature of the particle-size in figure 2.1b, and it is a peak of the intensity when the particle size is close to 95 μm . An intensity is approximately linear increasing with particle size

while the particle size is less than 95 μm , and it is an inverse relation between intensity and size while the particle size is larger than 95 μm . Similar features of the particle-size dependence are exhibited by powders of quartz ($\alpha\text{-SiO}_2$) as illustrated in the inset of figure 2.1b, which indicates that $\text{Ba}_8\text{Sn}_4\text{S}_{15}$ and $\alpha\text{-SiO}_2$ are not phase-matching materials on the basis of SHG measurements in powders⁷⁰. By the comparisons of the intensity localized at the peak between $\text{Ba}_8\text{Sn}_4\text{S}_{15}$ and $\alpha\text{-SiO}_2$, we can derive that the SHG intensity and SHG conversion efficient of $\text{Ba}_8\text{Sn}_4\text{S}_{15}$ are separately about 250 times than those of $\alpha\text{-SiO}_2$, and we also can find that the SHG intensity and SHG conversion efficient are separately about 10 times than those of AgGaS_2 at the particle size of 25–45 μm from figure 2.1b.

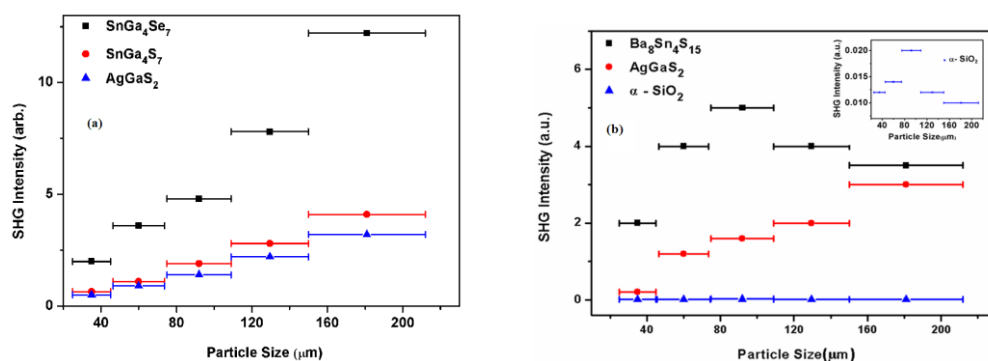


Figure 2.1. The SHG intensity vs. particle size of powders (a) SnGa_4G_7 ($G = \text{S}, \text{Se}$) and AgGaS_2 ; (b) $\text{Ba}_8\text{Sn}_4\text{S}_{15}$, $\alpha\text{-SiO}_2$ (inset panel), and AgGaS_2 .

Figure of merit and nonlinear optical coefficient

In accordance with formula (1), the SHG intensity $I_{2\omega}$ is direct proportion to the NLO coefficient d_{eff}^2 and is inverse proportion to refractive indexes ($n_{2\omega}^2$). And, both the refractive index and NLO coefficient are inverse relations with the band gaps. The figure of merit (FOM) is a balance indication of contradiction contributions between the refractive index and NLO coefficient, and well describes the quality of material-self. The FOM relative value between the sample and reference can be derived from the plots of SHG intensity vs. particle size, furthermore, the NLO coefficient of sample can be estimated from $d_{\text{eff}}^S \approx (I_{2\omega}^S/I_{2\omega}^R)^{1/2} d_{\text{eff}}^R$ from the FOM relative value when omitting the differences of refractive n between the sample and reference. The $FOMs$ of SnGa_4G_7 ($G = \text{S}, \text{Se}$) are about 1.3 and 3.8 times than that of AgGaS_2 , and their SHG coefficients d_{eff} are estimated to be 15.85 and 27.10 pm/V, respectively, with AgGaS_2 ($d_{\text{eff}}^R = 13.9$ pm/V⁷¹) as a reference in figure 2.1a⁶³. The theoretical values of the SHG coefficient d are also obtained by using the velocity-gauge formula derived by Sipe et al.⁶⁷. The space groups of SnGa_4G_7 ($G = \text{S}, \text{Se}$) crystals belong to class m , and there are ten nonvanishing tensors (d_{11} , d_{12} , d_{13} , d_{15} , d_{24} , d_{26} , d_{31} , d_{32} , d_{33} , and d_{35}) of second-order susceptibility. Judging from Kleinman's symmetry, only six independent tensor components (d_{11} , d_{12} , d_{13} , d_{15} , d_{24} , and d_{33}) are taken into account in the calculations, and the calculated values are listed in Table 1. The largest and smallest components (d_{33} and d_{12}) are calculated to be 37.51 and -1.77 pm/V for SnGa_4Se_7 , and to be 15.70

and -2.39 pm/V for SnGa_4S_7 at a wavelength of 2.05 μm , respectively. The largest components of calculations are the same order of magnitude as the experimental estimation for SnGa_4G_7 ($\text{G} = \text{S}, \text{Se}$).

The *FOM* of $\text{Ba}_8\text{Sn}_4\text{S}_{15}$ is 250 times than that of $\alpha\text{-SiO}_2$ and the SHG coefficient d_{eff} is estimated to be 6.39 pm/V in the intensity of localized at the peak (i.e. particle size of 95 μm) with $\alpha\text{-SiO}_2$ ($d_{\text{eff}}^{\text{R}} = 0.30$ pm/V⁷²) as a reference in figure 2.1b⁶⁵. Additionally, the *FOM* of $\text{Ba}_8\text{Sn}_4\text{S}_{15}$ is 1.12 times than that of AgGaS_2 and the SHG coefficient d_{eff} is estimated to be 14.71 pm/V in the intensity at particle size of 180 μm with AgGaS_2 ($d_{\text{eff}}^{\text{R}} = 13.9$ pm/V⁷¹) as a reference in figure 2.1b⁶⁵. The space group of $\text{Ba}_8\text{Sn}_4\text{S}_{15}$ belongs to class mm2, and there are five nonvanishing tensors (d_{15} , d_{24} , d_{31} , d_{32} , and d_{33}) of second-order susceptibility. Under the restriction of Kleinman's symmetry, only three independent SHG tensor components (d_{31} , d_{32} , and d_{33}) are considered. The calculated frequency-dependent SHG coefficients d_{31} , d_{32} , and d_{33} are plotted in figure 2.2 based on classical anharmonic oscillator model^{65, 66b}. It is found from figure 2.2 that the theoretical values of d_{31} , d_{32} , and d_{33} are about 23.97 , 21.97 , and 23.92 pm/V at a wavelength of 2.05 μm (0.60 eV), respectively. Noted here, the theoretical SHG coefficients d_{ij} only come from the electronic contributions, no including the contributions from lattice vibrations; and the measured SHG coefficients d_{ij} of powder depend on the particle size. Accordingly, the estimated value of d_{eff} based on the experimental measurement must come from the saturate particle size, i.e. SHG intensity is independent with the variation of particle size.

Table 1. Theoretical SHG coefficients d_{ij} (pm/V) at a wavelength 2.05 μm .

Compounds	d_{11}	d_{12}	d_{13}	d_{15}	d_{24}	d_{33}
SnGa_4S_7	-6.82	-2.39	-3.54	9.12	-10.19	15.70
SnGa_4Se_7	-4.82	-1.77	-5.54	18.84	-13.80	37.51

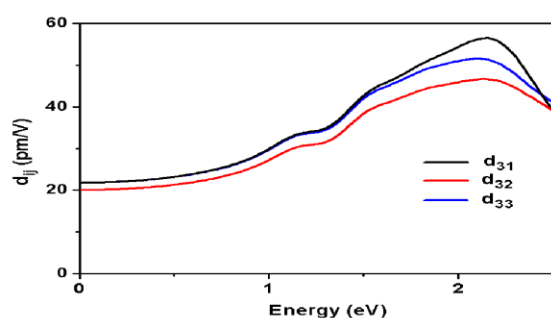


Figure 2.2. The calculated frequency-dependent second harmonic generation tensor components for $\text{Ba}_8\text{Sn}_4\text{S}_{15}$.

Laser induced damage thresholds

The damage threshold of material is also an important evaluation condition for a good quality NLO material. The damage threshold value is related to the parameters I_{ω} and λ_{ω} written in formula (1). The materials with higher damage threshold can allow to be illuminated by high

intensity of laser, and this material will have a large SHG conversion efficiency. It was reported that the laser damage probability depends on the fluency⁷³⁻⁷⁵. It was given that the fluence or energy density (J/cm^2) is ~~is relation~~ relates with the electric field (E_0^2) and incident wavelength λ ⁷³. Here, a single pulse laser induced damage threshold (LIDT) is employed to evaluate the powder damage threshold⁷⁶. The same particle size of samples SnGa_4G_7 ($G = \text{S}, \text{Se}$), $\text{Ba}_8\text{Sn}_4\text{S}_{15}$ and reference AgGaS_2 were packaged into the disks with a diameter of 8 mm. The optical microscope was used to observe the changes of the compounds when high-power 1064 nm laser radiation passed with a pulse width τ_p of 8 ns. The power of the laser beam was measured by a Nova II sensor, and the damage spot was measured using a Vernier caliper. Then the recorded laser power and the measured area of the damage spot were used to derive the LIDT values of the samples SnGa_4G_7 ($G = \text{S}, \text{Se}$), $\text{Ba}_8\text{Sn}_4\text{S}_{15}$ and reference AgGaS_2 , respectively^{63,65}. The results of powder LIDTs using single pulse measurement for these samples and reference are summarized in Table 2. The values in brackets are corresponding to particle size range (25–45 μm) of $\text{Ba}_8\text{Sn}_4\text{S}_{15}$ and AgGaS_2 , and the other values are corresponding to particle size (150–210 μm) of SnGa_4S_7 , SnGa_4Se_7 and AgGaS_2 at Table 2. The comparisons between the sample and reference would be made under the same experimental conditions. Accordingly, we find that the LIDT of $\text{Ba}_8\text{Sn}_4\text{S}_{15}$ ($122.1 \text{ MW}/\text{cm}^2$) is about 26 times than that of AgGaS_2 ($4.6 \text{ MW}/\text{cm}^2$), and the LIDTs of SnGa_4S_7 ($165.1 \text{ MW}/\text{cm}^2$) and SnGa_4Se_7 ($40.0 \text{ MW}/\text{cm}^2$) are about 19 and 4.6 times that of AgGaS_2 ($8.6 \text{ MW}/\text{cm}^2$), respectively. The high LIDTs imply that these materials are promising for high-power NLO application in the IR region.

Table 2. Results of powder LIDT measurements for compounds

Compound	damage energy (mJ)	spot diameter (mm)	damage threshold (MW/cm^2)
SnGa_4S_7	49.83	3.1	165.1
SnGa_4Se_7	34.00	5.2	40.0
$\text{Ba}_8\text{Sn}_4\text{S}_{15}$	55.37	3.8	122.1
AgGaS_2	12.13 (10.05)	6.7 (8.3)	8.6 (4.6)

Micro mechanism of NLO response for infrared materials

Band structures and density of states

The structures of energy bands are used to determine the optical gap and transparent zone, and the transport properties of material. The densities of states near to Fermi level are employed to determine the atomic or group charge distribution, and to analyze the process of charge transfers and the electronic origin of NLO response. The calculated band structures along the special k-point in the first Brillouin zone (BZ) and the partial density of states (PDOS) and total density of states (TDOS) are plotted in Figure 2.3 for $\text{Ba}_2\text{BiInS}_5$ compound⁶¹. It is found from Figure 2.3a that the valence band maximum (VBM) is located at the middle of the Γ --S line, while the

conduction band minimum (CBM) is located at the Γ point, indicating an indirect band gap of 1.61 eV for $\text{Ba}_2\text{BiInS}_5$ compound. It is found from figure 2.3b that the highest occupied states ranging from -4.0 to 0.0 eV (Fermi level) mainly contain S-3p states with small mixtures of Bi-6s6p and In-5s5p states; the lowest unoccupied states from 1.6 eV to 4.5 eV strongly involve unoccupied Bi-6p states and less unoccupied In-5s5p states. Thus, the charge transfers from occupied S-3p states to unoccupied Bi-6p states and to the hybridized In-5s5p states are believed to make main contributions to the optical absorption. We can see from PDOS that the dominant contribution to Bi-6s state is found at the lower energy range of -8.0 to -9.4 eV, and that the indirect mixing between Bi-6s and Bi-6p states is mediated by hybridization with S-3p states at the top of valence band for $\text{Ba}_2\text{BiInS}_5$ compound. Although the hybridized states of Bi-6s with S-3p close to the Fermi level account for only a small fraction of the total Bi-6s states, they play an important and crucial role in the formation of the Bi-6s stereochemically active lone-pair electron. These results show that the formation of the $\text{Bi}^{3+} 6s^2$ lone pair has dependence on the S^{2-} anion, and this dependence on the electronic states of the anion is evidence of the stereochemically active lone pair. It can be also found another evidence of the stereochemically active lone-pair electron based on partial electron density (PED) of 2.4⁶¹. The PEDs of the states from -2.5 to 0.0 eV (Fermi level) were calculated for $\text{Ba}_2\text{BiInS}_5$ compound, and plotted in Figure 2.4. Two dimensional electron density slices containing Bi and S atoms are shown through the (001) plane. An almost spherical electron distribution can be seen around the S atoms, and an asymmetric density distribution is clearly present around each Bi atom which directs away from their nearest-neighbor S atom. This finding indicates that there are the stereochemically active Bi^{3+} lone pairs. The stereochemically active Bi^{3+} lone pairs manifest in parallel local dipole alignment fashions and the cooperative effects of all local dipoles lead to the enhancement of macroscopic dipole moments. This is micro origin leading to a large SHG response of $\text{Ba}_2\text{BiInS}_5$ compound. Figure 2.5 gives the plots of the calculated band structures and densities of states of the $\text{Ba}_7\text{Sn}_5\text{S}_{15}$ ⁶². It is found from Figure 2.5a that this compound is an indirect band-gap material with a gap of 2.14 eV. From Figure 2.5b, we find that the band just above the Fermi level is predominately derived from Sn-5p states in group $[\text{Sn}_2\text{S}_3]^{2-}$, and is also small contributions from Sn-5s and S-3p states in group $[\text{SnS}_4]^{4-}$. However, the band just below the Fermi level is mostly composed of S-3p states in $[\text{Sn}_2\text{S}_3]^{2-}$ and $[\text{SnS}_4]^{4-}$ groups, respectively. Accordingly, the charge transfers across the band-gap edge originate from the (Sn_2S_3) and (SnS_4) polyhedrons, respectively.

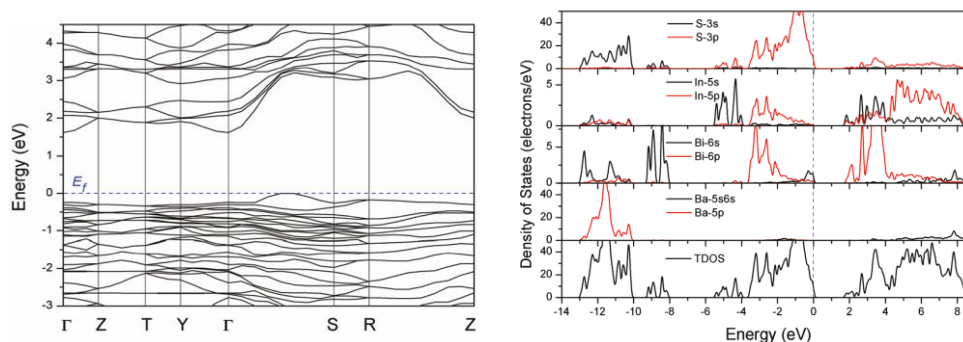


Figure 2.3. (a) The band structures and (b) total and partial density of states for $\text{Ba}_2\text{BiInS}_5$ using the norm-conserving pseudopotential method. The Fermi level is set at 0.0 eV.

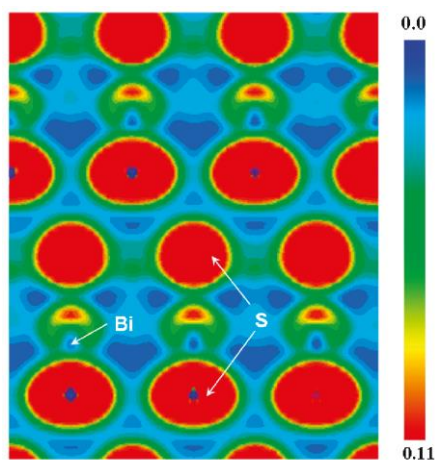


Figure 2.4. The partial electron density maps for compound $\text{Ba}_2\text{BiInS}_5$, and the electron density is represented from blue ($0.0 \text{ e}/\text{\AA}^3$) to red ($0.11 \text{ e}/\text{\AA}^3$). The above DFT calculations were performed by using the PAW potential method.

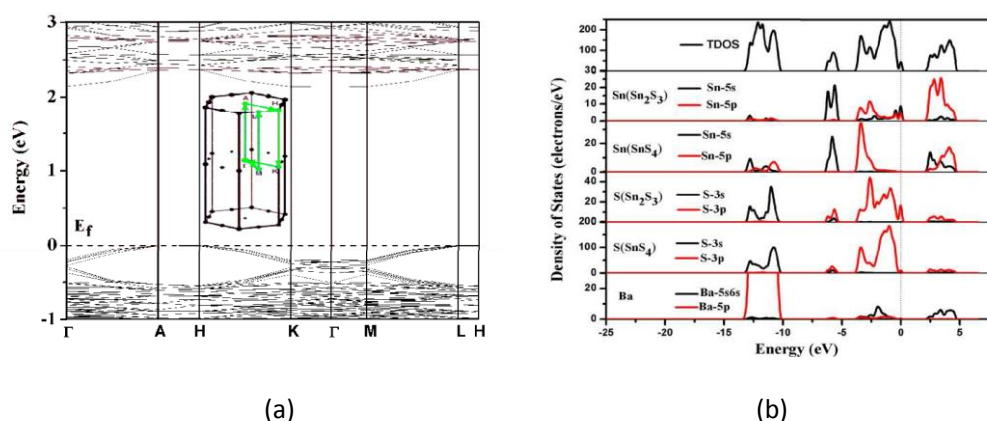


Figure 2.5. (a) The band structures and (b) density of states for $\text{Ba}_7\text{Sn}_5\text{S}_{15}$ compound

Local dipole moment

The local dipole moments of $[\text{Sn}_2\text{S}_3]^{2-}$ and $[\text{SnS}_4]^{4-}$ is 2.1287, 0.9547 Debye, respectively in $\text{Ba}_7\text{Sn}_5\text{S}_{15}$ compound based on the electronic structural calculations of isolate groups⁶². These results show that the polarization is much larger for the isolate trigonal-bipyramidal $[\text{Sn}_2\text{S}_3]^{2-}$ than for the isolate tetrahedral $[\text{SnS}_4]^{4-}$ in $\text{Ba}_7\text{Sn}_5\text{S}_{15}$ material. Accordingly, we consider that the group (Sn_2S_4) makes a most of contribution to the NLO response of $\text{Ba}_7\text{Sn}_5\text{S}_{15}$ material. Figure 2.6a gives the top view of the electron density contour surface for isolate $[\text{Sn}_2\text{S}_3]^{2-}$, and it indicates the charge transfers from S^{2-} to Sn^{2+} ions. Figure 2.6b gives the plots of group $[\text{Sn}_2\text{S}_3]^{2-}$ arrangements in the $\text{Ba}_7\text{Sn}_5\text{S}_{15}$ crystal, and it is found ~~finds~~ that the dipole origination of $[\text{Sn}_2\text{S}_3]^{2-}$ along the z direction is parallel to each other. The polarity superposition of the $[\text{Sn}_2\text{S}_3]^{2-}$ groups will strengthen the crystal polarity and lead to a large SHG response of a crystal material $\text{Ba}_7\text{Sn}_5\text{S}_{15}$.

Table 3 lists the local dipole moments of the $[\text{SnS}_3]^{4-}$ and $[\text{SnS}_4]^{4-}$ anionic groups within $\text{Ba}_8\text{Sn}_4\text{S}_{15}$ compound based on the calculations of *ab initio* method with the Gaussian03 package⁶⁵. The obtained results show that the polarization of the isolate pyramidal $[\text{SnS}_3]^{4-}$ is much larger than that of the isolate tetrahedral $[\text{SnS}_4]^{4-}$. The average dipole moments of the $[\text{SnS}_4]^{4-}$ and total dipole moments of 6 $[\text{SnS}_4]^{4-}$ groups in the unit cell are 1.8305 and 10.9832 Debye, respectively, and the average dipole moments of $[\text{SnS}_3]^{4-}$ and total dipole moments of 2 $[\text{SnS}_3]^{4-}$ anions are 11.7229 and 23.4459 Debye, respectively in the unit cell of $\text{Ba}_8\text{Sn}_4\text{S}_{15}$ compound. A large dipole moment of $[\text{SnS}_3]^{4-}$ anion is attributed to its pyramidal geometry, which has the lone pair electrons of stereochemical activity. Thus, the $[\text{SnS}_3]^{4-}$ anions can make more contribution than the $[\text{SnS}_4]^{4-}$ anions to the NLO response of $\text{Ba}_8\text{Sn}_4\text{S}_{15}$.

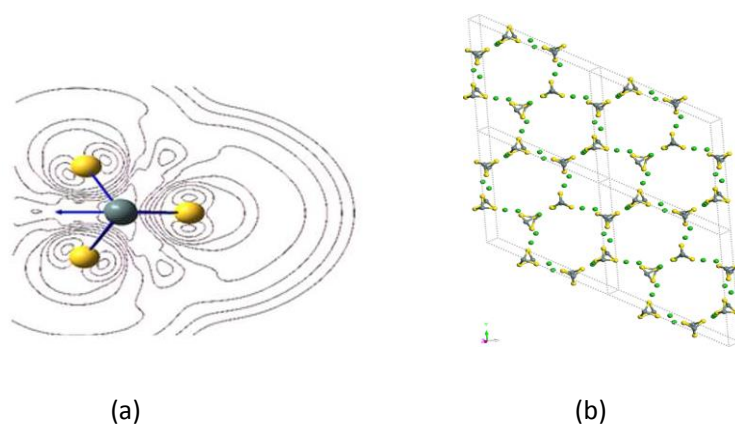


Figure 2.6. (a) The top view of electron density contour surface and the dipole moment for isolate $[\text{Sn}_2\text{S}_3]^{2-}$. (b) The arrangement of $[\text{Sn}_2\text{S}_3]^{2-}$ in a 2x2 unit cell for the $\text{Ba}_7\text{Sn}_5\text{S}_{15}$ crystal, the $[\text{SnS}_4]^{2-}$ group was not shown for clarity. Atom color: S: yellow, Sn: gray, Ba: green.

Table 3. Calculative Dipole Moment of $[\text{SnS}_4]^{4-}$ and $[\text{SnS}_3]^{4-}$ Anions

Anion group	dipole moment (Debye)
$[\text{Sn}(1)\text{S}_4]^{4-}$	1.2359
$[\text{Sn}(2)\text{S}_4]^{4-}$	3.0696
$[\text{Sn}(3)\text{S}_4]^{4-}$	1.8126
$[\text{Sn}(4)\text{S}_4]^{4-}$	1.5062
$[\text{Sn}(5)\text{S}_4]^{4-}$	2.0640
$[\text{Sn}(6)\text{S}_4]^{4-}$	1.2949
$[\text{Sn}(7)\text{S}_3]^{4-}$	11.8679
$[\text{Sn}(8)\text{S}_3]^{4-}$	11.5780

Summary and Prospect

We describe the optimization of NCS chromophore of materials, and present a way of designing syntheses of inorganic NCS compounds based on the normal processes of development of NCS chromophores. We introduce the alienation process of NCS chromophore development while the NCS compound is not formed by NCS chromophore. We illustrate these concepts by taking actual examples. The NCS chromophores of (SnS_4) and (Sn_2S_3) were normal development

to obtain the NCS crystal of $\text{Ba}_7\text{Sn}_5\text{S}_{15}$. The NCS chromophores of (BiS_3) and (InS_4) were development into a compound of $\text{Ba}_2\text{BiInS}_5$ keeping in NCS structure. The NCS crystals SnGa_4Q_7 ($\text{Q} = \text{S}, \text{Se}$) were obtained by NCS chromophores of (GaQ_4) and (SnQ_4) . On the contrary, the CS compound of $\text{Ba}_6\text{Sn}_7\text{S}_{20}$ was obtained because the developments of NCS chromophores of the (SnS_4) and (SnS_5) alienate from the normal process of growth. We give more examples of NCS chromophore developments which are normal or alienable process of chromophore growth in this paper. Here, we only describe the inorganic NCS chalcogenides which are constructed by two chromophores. And they are constructed by three or multiple NCS chromophores which would be obtained basis on the present method.

For NCS compounds, we investigate their NLO properties of micro-crystals (powders) and electronic origin of NLO response in views of the calculations and simulations. The SHG intensity, laser-induced damage threshold, and infrared transparency were measured. Furthermore, the relative conversion efficiency and figure of merit are derived based on SHG intensity measurements. The calculated charge distributions and local dipole are employed to evaluate the micromechanism of NCS materials. It is found that the NCS materials of SnGa_4Q_7 ($\text{Q} = \text{S}, \text{Se}$) appear with large conversion efficiencies, high damage threshold and wide transparencies in the mid-infrared region. And, the study of micro-mechanism elucidate that the stereochemically active lone-pair electrons of Sn^{2+} can significantly improve the polarity of the $[\text{SnQ}_4]$ chromophore. Large NLO responses of them originate from the covalent interactions of $\text{Sn}-\text{Q}$ and the cooperative effects of polarities between the $[\text{SnQ}_4]$ and $[\text{GaQ}_4]$ chromophores. It is also found that the $\text{Ba}_7\text{Sn}_5\text{S}_{15}$ material is type-I phase-matchability, and that the SHG conversion efficiency and figure of merit are about twice of that of AgGaS_2 at the saturated particle size (particle size of 150–212 μm). The $\text{Ba}_8\text{Sn}_4\text{S}_{15}$ is not phase-matching material. The SHG intensity and conversion efficient of $\text{Ba}_8\text{Sn}_4\text{S}_{15}$ are separately about 250 times than those of $\alpha\text{-SiO}_2$, and the SHG intensity and conversion efficient are separately about 10 times than those of AgGaS_2 at the particle size of 25–45 μm .

~~On the basis of considering~~ Based upon the requirements of high quality NLO crystals, we believe that the NLO crystals of SnGa_4Q_7 ($\text{Q} = \text{S}, \text{Se}$) are in full compliance with the mentioned requirements and they are good candidates to be applied in laser frequency conversion of mid-infrared zone. In the future, the key work is to grow the single crystals with size of larger than 10 mm at one hand, and on the other hand, ~~the work is seeks~~ we try to prepare the transparent film with NLO response.

Acknowledgements

This investigation was based on work supported by the National Basic Research Program of China (grant no. 2014CB845605), the National Natural Science Foundation of China (21173225, 91222204 and 21101156).

Notes and References

State Key Laboratory of Structural Chemistry, Fujian Institute of Research on the Structure of Matter, Chinese Academy of Sciences, Fuzhou, Fujian, 350002, PRC. Fax:(+86)591-83714946,Tel:(+86)591-83713068. E-Mail: cwd@fjirsm.ac.cn

1. N. Setter, D. Damjanovic, L. Eng, G. Fox, S. Gevorgian, S. Hong, H. Kohlstedt, A. Kingon, N. Park, G. Stephenson, I. Stolitchnov, A. K. Tagantsev, D.V. Taylor, T. Yamada, S. Streiffer, *J. Appl. Phys.*, 2006, **100**, 051606.
2. P. S. Halasyamani, K. R. Poeppelmeier, *Chem. Mater.*, 1998, **10**, 2753.
3. A. M. Glazer, K. Stadnicka, *Acta Crystallogr.*, 1989, **A45**, 234.
4. T. Hahn, *International Tables for Crystallography*. D. Reidel Publishing Company, Dordrecht, 1983.
5. Frank K. Tittle, Dirk Richter, Alan Fried, *Solid-State Mid-Infrared Laser Sources Topics in Applied Physics*, 2003, **89**, 458, <http://link.springer.com/book/10.1007/3-540-36491-9>.
6. Jun Sakuma, Koichi Moriizumi, Haruhiko Kusunose, *Optics Express*, 2011, **19**,15020.
7. H. Zhang, G. Wang, L. Guo, A. Geng, Y. Bo, D. Cui, Z. Xu, R. Li, Y. Zhu, X. Wang, C. Chen, *Applied Physics B*, 2010, **93**,323.
8. K. Kuroda, Y. Toya, T. Satoh, T. Shimura, S. Ashihara, Y. Takahashi, M. Yoshimura, Y. Mori and T. Sasaki, *Journal of Physics: Conference Series*, 2010, **206**, 012014.
9. R. A. Kaindl, M. Wurm, K. Reimann, P. Hamm, A. M. Weiner, and M. Woerner, *J. Opt. Soc. Am. B*, 2000, **17**, 12.
10. A. Miklos, C.H. Lim, W.W. Hung, G.C. Liang, A.H. Kung, A. Schmohl, P. Hess, *Applied Optics*, 2002, **41**, 2985.
11. J. Kottmann, J. M. Rey, J. Luginbuehl, E. Reichmann, and M. W. Sigrist, *Biomedical Optics Express*, 2012, **3**, 667.
12. Y. Braiman, www.ornl.gov.
13. Reiner Hennig, Monika Maintz, *The Herschel space telescope*, www.esa.int/education.
14. Yisa Rumala, *The York Scholar*, 2006, **3**, 52.
15. I. Chung, C. D. Malliakas, J. I. Jang, C. G. Canlas, D. P. Weliky, M. G. Kanatzidis, *J. Am. Chem. Soc.*, 2007, **129**, 14996.
16. I. Chung, J.-H. Song, J. I. Jang, A. J. Freeman, M. G. Kanatzidis, *J. Solid State Chem.*, 2012, **195**, 161.
17. (a) C. D. Morris, I. Chung, S. Park, C. M. Harrison, D. J. Clark, J. I. Jang, M. G. Kanatzidis, *J. Am. Chem. Soc.*, 2012, **134**, 20733; (b) J. I. Jang, S. Park, C. M. Harrison, D. J. Clark, C. D. Morris, I. Chung, M. G. Kanatzidis, *Opt. Lett.*, 2013, **38**, 1316.
18. J. A. Aitken, G. A. Marking, M. Evain, L. Iordanidis, M. G. Kanatzidis, *J. Solid State Chem.*, 2000, **153**, 158.
19. D. J. Mei, W. L. Yin, K. Feng, Z. S. Lin, L. Bai, J. Y. Yao, Y. C. Wu, *Inorg. Chem.*, 2012, **51**,

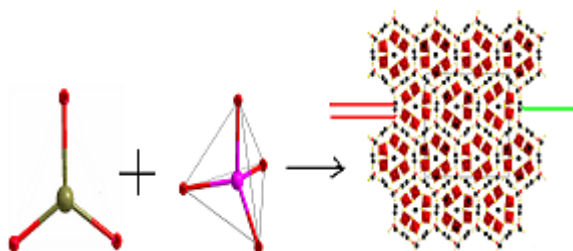
- 1035.
20. J. H. Liao, G. M. Marking, K. F. Hsu, Y. Matsushita, M. D. Ewbank, R. Borwick, P. Cunningham, M. J. Rosker, M. G. Kanatzidis, *J. Am. Chem. Soc.*, 2003, **125**, 9484.
21. W. Yin, K. Feng, W. Hao, J. Yao, Y. Wu, *Inorg. Chem.*, 2012, **51**, 5839.
22. J. W. Lekse, M. A. Moreau, K. L. McNerny, J. Yeon, P. S. Halasyamani, J. A. Aitken, *Inorg. Chem.*, 2009, **48**, 7516.
23. K. Feng, X. X. Jiang, L. Kang, W. L. Yin, W. Y. Hao, Z. S. Lin, J. Y. Yao, Y. C. Wu, C. T. Chen, *Dalton Trans.*, 2013, **42**, 13635.
24. M. J. Manos, J. I. Jang, J. B. Ketterson, M. G. Kanatzidis, *Chem. Commun.* 2008, 972.
25. N. Ding, D.-Y. Chung, M. G. Kanatzidis, *Chem. Commun.*, 2004, 1170.
26. N. Ding, M. G. Kanatzidis, *Angew. Chem., Int. Ed.*, 2006, **45**, 1397.–1401.
27. (a) M. J. Manos, K. Chrissafis, M. G. Kanatzidis, *J. Am. Chem. Soc.*, 2006, **128**, 8875; (b) M. J. Manos, R. G. Iyer, E. Quarez, J. H. Liao, M. G. Kanatzidis, *Angew. Chem., Int. Ed.*, 2005, **44**, 3552.
28. X. Lin, Y. Guo, N. J. Ye, *Solid State Chem.*, 2012, **195**, 172.
29. Y. K. Chen, M. C. Chen, L. J. Zhou, L. Chen, L. M. Wu, *Inorg. Chem.*, 2013, **52**, 8334.
30. S. M. Kuo, Y. M. Chang, I. Chung, J. K. Jang, B. H. Her, S. H. Yang, J. B. Ketterson, M. J. Kanatzidis, K. F. Hsu, *Chem. Mater.*, 2013, **25**, 2427.
31. A. H. Reshak, I. V. Kityk, O. V. Parasyuk, H. Kamarudin, S. Auluck, *J. Phys. Chem. B*, 2013, **117**, 2545.
32. A. H. Reshak, Y. M. Kogut, A. O. Fedorchuk, O. V. Zamuruyeva, G. L. Myronchuk, O. V. Parasyuk, H. Kamarudin, S. Auluck, K. J. Plucinski, J. Bila, *Phys. Chem. Chem. Phys.*, 2013, **15**, 18979.
33. Y. Kim, S. W. Martin, K. M. Ok, P. S. Halasyamani, *Chem. Mater.*, 2005, **17**, 2046.
34. Hua Lin, Ling Chen, Liu-Jiang Zhou, Li-Ming Wu, *J. Am. Chem. Soc.*, 2013, **135**, 12914.
35. Qi Wu, Xianggao Meng, Cheng Zhong, Xingguo Chen, and Jingui Qin *J. Am. Chem. Soc.*, 2014, **136**, 5683.
36. Valentin Petrov, *Optical Materials*, 2012, **34**, 536.
37. I. Chung and M. G. Kanatzidis, *Chem. Mater.*, 2014, **26**, 849.
38. O. R. Evans, W. Lin, *Chem. Mater.* 2001, **13**, 2705.
39. S. D. Bells, M. A. Ratner, T. J. Marks, *J. Am. Chem. Soc.*, 1992, **114**, 5842.
40. T. K. Bera, J. I. Jang, J. B. Ketterson, M. G. Kanatzidis, *J. Am. Chem. Soc.*, 2009, **131**, 75.
41. H. S. Ra, K. M. Ok, P. S. Halasyamani, *J. Am. Chem. Soc.*, 2003, **125**, 7764.
42. R. E. Sykora, K. M. Ok, P. S. Halasyamani, T. E. Albrecht-Schmitt, *J. Am. Chem. Soc.*, 2002, **124**, 1951.
43. (a) E. O. Chi, K. M. Ok, Y. Porter, P. S. Halasyamani, *Chem. Mater.*, 2006, **18**, 2070; (b) D. Phanon, I. Gautier-Luneau, *Angew. Chem., Int. Ed.*, 2007, **46**, 8488.
44. F. Kong, S.P. Huang, Z.-M. Sun, J. G. Mao, W.-D. Cheng, *J. Am. Chem. Soc.*, 2006,

128,7750.

45. Y. Inaguma, M. Yoshida, T. Katsumata, *J. Am. Chem. Soc.*, 2008, **130**, 6704.
46. S.-H. Kim, J. Yeon, P. S. Halasyamani, *Chem. Mater.*, 2009, **21**, 5335.
47. D. Phanon, I. Gautier-Luneau, *Angew. Chem., Int. Ed.*, **2007**, *46*, 8488.
48. H.-Y. Chang, S.-H. Kim, K. M. Ok, P. S. Halasyamani, *J. Am. Chem. Soc.*, 2009, **131**, 6865.
49. G.-H. Zou, L. Huang, N. Ye, C.-S. Lin, W.-D. Cheng, H. Huang *J. Am. Chem. Soc.*, 2013, **135**, 18560.
50. Y. Kim, S. W. Martin, K. M. Ok, P. S. Halasyamani, *Chem. Mater.*, 2005, **17**, 2046.
51. V. V. Badikov, A. G. Tyulyupa, G. S. Shevyrdyaeva, S. G. Sheina, *Inorg. Mater.*, 1991, **27**, 177 [Translation from *Dokl. Akad. Nauk SSSR, Neorg. Mater.*, 1991, **27**, 248.].
52. (a) Y. Kim, I.-seok Seo, S. W. Martin, J. Baek, P. S. Halasyamani, N. Arumugam, H. Steinfink, *Chem. Mater.*, 2008, **20**, 6048; (b) T. Yang, J. Sun, J. Yeon, P. S. Halasyamani, S. Huang, J. Hemberger, M. Greenblatt, *Chem. Mater.*, 2010, **22**, 4814.
53. W.-L. Zhang, W.-D. Cheng, H. Zhang, L. Geng, C.-S. Lin, Z.-Z. He, *J. Am. Chem. Soc.*, 2010, **132**, 1508.
54. <http://materialsinnovation.tms.org/genome.aspx> *Materials Genome Initiative for Global Competitiveness*, published by the National Science and Technology Council.
55. P. A. Maggard, C. L. Stern, K. R. Poeppelmeier, *J. Am. Chem. Soc.*, 2001, **123**, 7742.
56. M. E. Well, A. Norquist, F. P. Arnold, C. L. Stern, K. R. Poeppelmeier, *Inorg. Chem.*, 2002, **41**, 5119.
57. P. A. Maggard, T. S. Nault, K. R. Poeppelmeier, *J. Solid State Chem.*, 2003, **175**, 27.
58. H. K. Izumi, J. E. Kirsch, C. L. Stern, K. R. Poeppelmeier, *Inorg. Chem.*, 2005, **44**, 884.
59. M. R. Marvel, J. Lesage, J. Baek, P. S. Halasyamani, C. L. Stern, K. R. Poeppelmeier, *J. Am. Chem. Soc.*, 2007, **129**, 13963.
60. H. Y. Chang, S. H. Kim, K. M. Ok, P. S. Halasyamani, *J. Am. Chem. Soc.*, 2009, **131**, 6865.
61. L. Geng, W.-D. Cheng, C.-S. Lin, W.-L. Zhang, H. Zhang, Z.-Z. He, *Inorg. Chem.*, 2011, **50**, 5679.
62. Z.-Z. Luo, C.-S. Lin, W.-D. Cheng, H. Zhang, W.-L. Zhang, Z.-Z. He, *Inorg. Chem.*, 2013, **52**, 273.
63. Z.-Z. Luo, C.-S. Lin, H.-H. Cui, W.-L. Zhang, H. Zhang, Z.-Z. He, W.-D. Cheng, *Chem. Mater.*, 2014, **26**, 2743.
64. B. Cordero, V. Gomez, A. E. Platero-Prats, M. Reves, J. Echererria, E. Cremades, F. Barragan, S. Alvarez, *Dalton Trans.*, 2008, 2832-2838.
65. Z.-Z. Luo, C.-S. Lin, W.-L. Zhang, H. Zhang, Z.-Z. He, W.-D. Cheng, *Chem. Mater.*, 2014, **26**, 1093.
66. Robert W. Boyd, *Nonlinear Optics*, **third edition**, Academic Press, 2008, (a) p.69-79; (b) p.22—33.
67. (a) D. J. Moss, E. Ghahramani, J. E. Sipe, H. M. van Driel, *Phys. Rev. B*, 1990, **41**, 1542, (b) James L. P. Hughes, J. E. Sipe, *Phys. Rev. B*, 1996, **53**, 10 751.

68. K. M. Ok, E. Ok Chi, P. S. Halasyamani, *Chem. Soc. Rev.*, 2006, **35**, 710.
69. G. Kortüm, *Reflectance Spectroscopy*; Springer-Verlag: New York, 1969.
70. S. K. Kurtz, T. T. Perry, *J. Appl. Phys.* 1968, **39**, 3798.
71. J.-J. Zondy, D. Touahri, O. Acef, *J. Opt. Soc. Am. B*, 1997, **14**, 2481.
72. D. A. Roberts, *IEEE J.* 1992, **28**, 2057.
73. J.-Y. Natoli, L. Gallais, H. Akhouayri, C. Amra, *Appl. Optics*, 2002, **41**, 3156.
74. K. T. Zawilski, S. D. Setzler, P. G. Schunemann, T. M. Pollak, *J. Opt. Soc. Am. B*, 2006, **23**, 2310.
75. C. Xu, S. Yang, J.-F. Wang, J.-N. Niu, H. Ma, Y.-H. Qiang, J.-T. Liu, D.-W. Li, C.-X. Tao, *Chin. Phys. Lett.* 2012, **29**, 084207.
76. M. J. Zhang, X. M. Jiang, L. J. Zhou, L. G. C. Guo, *J. Mater. Chem. C*, 2013, **1**, 4754

Colour graphic:



Text:

The designs of NCS compounds based on normal development of NCS chromophore is presented and the NLO properties are investigated.

JOURNAL COVER OPPORTUNITY:

